

# Geophysical Research Letters<sup>®</sup>

## RESEARCH LETTER

10.1029/2025GL118562

### Key Points:

- We reveal the roles of plasma density variations and compressional magnetic field fluctuations in modulating chorus wave excitation
- Chorus modulation arises from nonlinear wave-particle interactions influenced by variations in background plasma parameters
- Electron precipitation driven by modulated chorus waves leads to the formation of pulsating aurora

### Supporting Information:

Supporting Information may be found in the online version of this article.

### Correspondence to:

H. Chen and X. Wang,  
[huayue\\_chen@foxmail.com;](mailto:huayue_chen@foxmail.com;)  
[wangxue@auburn.edu](mailto:wangxue@auburn.edu)

### Citation:

Chen, H., Wang, X., Chen, R., Chen, L., Omura, Y., Miyoshi, Y., et al. (2025). Simulation study of chorus wave modulation and associated electron precipitation. *Geophysical Research Letters*, 52, e2025GL118562. <https://doi.org/10.1029/2025GL118562>

Received 1 AUG 2025

Accepted 10 SEP 2025

## Simulation Study of Chorus Wave Modulation and Associated Electron Precipitation



Huayue Chen<sup>1</sup> , Xueyi Wang<sup>1</sup> , Rui Chen<sup>1</sup> , Lunjin Chen<sup>2</sup> , Yoshiharu Omura<sup>1,3</sup> , Yoshizumi Miyoshi<sup>4</sup> , Xiaolei Li<sup>1</sup> , and Yi-Kai Hsieh<sup>3</sup>

<sup>1</sup>Department of Physics, Auburn University, Auburn, AL, USA, <sup>2</sup>William B. Hanson Center for Space Sciences, University of Texas at Dallas, Richardson, TX, USA, <sup>3</sup>Research Institute for Sustainable Humanosphere, Kyoto University, Uji, Japan,

<sup>4</sup>Institute for Space-Earth Environmental Research, Nagoya University, Nagoya, Japan

**Abstract** The modulation of chorus waves on several-second timescales in Earth's magnetosphere plays a crucial role in modulating electron precipitation intensity, leading to the formation of pulsating aurora.

However, the physical mechanism underlying chorus modulation remains not fully understood. In this study, we perform self-consistent particle-in-cell simulations with typical magnetospheric plasma parameters to quantify chorus modulation driven by plasma density variations and compressional magnetic field fluctuations. It is demonstrated that chorus modulation is determined by nonlinear wave-particle interactions, in which the condition for nonlinear wave growth is highly sensitive to background plasma parameters. The resulting electron precipitation in the ~10–200 keV energy range exhibits modulation on comparable timescales, consistent with observations of pulsating aurora. This study enhances our understanding of how variations in magnetospheric plasma parameters influence chorus wave excitation and the associated particle dynamics.

**Plain Language Summary** Chorus waves are coherent whistler-mode emissions in Earth's magnetosphere that play a key role in driving electron precipitation, contributing to the loss of energetic electrons from the ring current and radiation belts. This precipitation causes pulsating aurora in the upper ionosphere, which can impact satellite navigation, radio communication, and power grid stability. Observations show that both chorus waves and the associated electron precipitation exhibit modulation on timescales of several seconds, attributed to variations in background plasma parameters. In this study, we perform self-consistent particle-in-cell simulations with typical magnetospheric plasma parameters to investigate the influences of plasma density variations and compressional magnetic field fluctuations on chorus wave excitation. The simulations reproduce the wave modulation and reveal that this modulation is controlled by nonlinear interactions with energetic electrons. Moreover, the simulated electron precipitation shows similar modulation with comparable periods, consistent with observations of pulsating aurora. This study highlights the critical role of background plasma variability in regulating nonlinear wave-particle interactions and contributes to a deeper understanding of magnetospheric dynamics.

## 1. Introduction

Chorus waves are coherent, narrowband whistler-mode emissions in Earth's magnetosphere, characterized by discrete rising-tone elements (Burtis & Helliwell, 1969; Horne & Thorne, 1998; Tsurutani & Smith, 1974). They play a crucial role in the loss of energetic electrons from the ring current and radiation belts by driving precipitation into the upper ionosphere (Gao et al., 2023; Kang et al., 2022; Kasahara et al., 2018; Miyoshi et al., 2020, 2021; Thorne et al., 2010). The resulting electron precipitation produces pulsating aurora (R. Chen et al., 2024; Jaynes et al., 2015; Miyoshi, Oyama, et al., 2015; Miyoshi, Saito, et al., 2015; Nishimura et al., 2010; Ozaki et al., 2018), which can affect satellite navigation (Chernous et al., 2018; Semeter et al., 2017), radio communication (Benson, 1960; Kellogg & Monson, 1979), and power grid stability (Albertson & Thorson, 1974; Boteler, 2019).

Chorus waves typically exhibit quasi-periodic modulation on timescales of several seconds, commonly referred to as chorus bursts (Agapitov et al., 2018; Nishimura et al., 2010; Tsurutani & Smith, 1974). This modulation is thought to arise from variations in background plasma parameters, including plasma density variations (W. Li, Bortnik, et al., 2011; Moullard et al., 2002; Nishimura et al., 2015; Xia et al., 2020) and compressional magnetic field fluctuations associated with ultra-low-frequency (ULF) waves (W. Li, Thorne, et al., 2011; L. Li et al., 2023; Xia et al., 2020; Zhang et al., 2019). Early studies proposed that chorus modulation results from linear growth rate changes due to modifications in resonant electron density (W. Li, Bortnik, et al., 2011; W. Li, Thorne, et al., 2011;

Nishimura et al., 2015). However, recent work has demonstrated that nonlinear wave-particle interactions play a key role in chorus excitation (H. Chen et al., 2023; R. Chen et al., 2025; Demekhov et al., 2020; Hanzelka & Santolík, 2023; Omura, 2021; Santolík et al., 2014; Wang et al., 2024). Therefore, the physical mechanism underlying chorus modulation remains not fully understood.

Electron precipitation driven by modulated chorus waves also exhibits periodic patterns, leading to alternating “on-off” brightness in pulsating aurora with several-second periods, known as main modulation (R. Chen et al., 2024; Miyoshi, Saito, et al., 2015; Hosokawa et al., 2020; Nishiyama et al., 2016). Test particle simulations are widely used to study this process (L. Chen et al., 2020; da Silva et al., 2018; Gan et al., 2020; Miyoshi, Oyama, et al., 2015; Miyoshi, Saito, et al., 2015; Miyoshi et al., 2020; O'Brian et al., 2022); however, they neglect the feedback from energetic electrons to waves and typically underestimate the precipitation intensity by approximately an order of magnitude (H. Chen et al., 2025). In contrast, self-consistent simulations, which capture wave excitation and particle scattering through fully coupled wave-particle interactions, produce precipitation intensities consistent with typical observations from low-Earth-orbit (LEO) satellites (Shen et al., 2023; Zhang et al., 2022, 2023).

In this study, we conduct self-consistent particle-in-cell (PIC) simulations with typical magnetospheric parameters. These simulations quantify the modulation of both chorus waves and the associated electron precipitation, driven separately by plasma density variations and compressional magnetic field fluctuations. We further demonstrate that chorus modulation is determined by nonlinear interactions with energetic electrons.

## 2. Simulation Model

We perform one-dimensional PIC simulations in a dipole magnetic field using the general curvilinear plasma simulation code (GCPIC) model (Lu et al., 2019; Wang et al., 2024). The simulation includes two electron populations: cold and energetic electrons. The  $\delta f$  method is applied by introducing the particle weight  $w \equiv \delta f/f$  to calculate the perturbed phase space density  $\delta f = f - f_0$  (Lu et al., 2021), where  $f$  is the instantaneous distribution and  $f_0$  is the initial distribution. Further details are provided in Parker and Lee (1993) and Hu and Krommes (1994). Energetic electrons are continuously injected into the simulation domain due to azimuthal drift in a dipole field, characterized by a drift timescale  $\tau_D$  (Lu et al., 2021). Absorbing boundary conditions are applied for electromagnetic fields, and reflecting boundary conditions are used for particles.

The simulation domain is constructed in a reduced system with a scaling factor of 10 at  $L = 6$  (H. Chen et al., 2025; Ke et al., 2022). The domain comprises 5,000 grid cells, spanning a magnetic latitude  $\lambda$  range from  $\sim -30^\circ$  to  $\sim 30^\circ$ . A schematic of the domain is shown in Figure S1 of Supporting Information S1. The nominal value of the equatorial background magnetic field is  $B_{e0} = 144$  nT (i.e.,  $31,200$  nT/6<sup>3</sup>), and the magnetic field along the field line follows a dipole topology given by  $B_{\text{dip}} = B_{e0}\sqrt{1 + \sin^2 \lambda}/\cos^6 \lambda$ . The plasma density is uniform along the field line, with a nominal value of  $n_{e0} = 5$  cm<sup>-3</sup> (Denton et al., 2004; Escoubet et al., 1997; W. Li, Bortnik, et al., 2011). Time is normalized to the inverse equatorial electron gyrofrequency  $\Omega_{e0}^{-1}$ , where  $\Omega_{e0} = eB_{e0}/m_e$ , with  $e$  denoting the elementary charge and  $m_e$  the electron mass. Spatial distance is normalized to  $V_{Ae0}/\Omega_{e0}$ , where  $V_{Ae0} = B_{e0}/\sqrt{\mu_0 n_{e0} m_e}$  is the electron Alfvén speed, and  $\mu_0$  is the vacuum permeability.

Energetic electrons are initialized with a subtracted Maxwellian distribution (Omura, 2021):

$$f(u_{\parallel}, u_{\perp}) = \frac{n_{\text{heq}}}{(2\pi)^{3/2} U_{\parallel} U_{t\perp}^2 (1 - \rho\beta)} \exp\left(-\frac{u_{\parallel}^2}{2U_{\parallel}^2}\right) \cdot \left[ \exp\left(-\frac{u_{\perp}^2}{2U_{t\perp}^2}\right) - \rho \exp\left(-\frac{u_{\perp}^2}{2\beta U_{t\perp}^2}\right) \right], \quad (1)$$

with parameters  $\rho = 1$  and  $\beta = 0.3$ . Here,  $n_{\text{heq}}$  is the equatorial number density,  $U_{\parallel}$  and  $U_{t\perp}$  denote the parallel and perpendicular thermal momentum, and  $u_{\parallel}$  and  $u_{\perp}$  are the parallel and perpendicular momentum. At the magnetic equator,  $n_{\text{heq}}$  is 0.075 cm<sup>-3</sup> (Gao et al., 2014; W. Li, Bortnik, et al., 2011; Rasinskaite et al., 2025), the parallel temperature is  $T_{\parallel} = m_e U_{\parallel}^2 = 20$  keV (Li, Bortnik, et al., 2011; W. Li, Thorne, et al., 2011; Rasinskaite et al., 2025), and the temperature anisotropy is  $T_{\perp}/T_{\parallel} = U_{t\perp}^2/U_{\parallel}^2 = 1.6$  (Fu et al., 2014; Yue et al., 2016), which are all typical magnetospheric values. The injection parameter is  $\Omega_{e0}\tau_D = 5,000$  (Gao et al., 2022). Cold electrons are initialized with a Maxwellian distribution with a temperature of 2 eV. The particle number per cell (ppc) is set to 600 for each species.

At the northern and southern boundaries of the simulation domain, electrons that enter the loss cone are removed and treated as precipitating electrons (H. Chen et al., 2025; Kong et al., 2025). The corresponding precipitation flux is evaluated at the magnetic footprints in both hemispheres, located at an altitude of 100 km above Earth's surface, with magnetic latitudes  $\lambda_{\text{FT}}^N$  and  $\lambda_{\text{FT}}^S$  representing the northern and southern upper ionosphere, respectively. The adiabatic motion of electrons along the magnetic field line from the simulation boundary to the upper ionosphere is considered.

Variations in the background magnetic field and plasma density have been observed during ULF waves (W. Li, Thorne, et al., 2011; L. Li et al., 2023). Some events, however, show changes in only one of these parameters (Xia et al., 2020). To isolate the roles of plasma density variations and compressional magnetic field fluctuations, we design two simulation cases. In Case I, the plasma density varies with time while the background magnetic field remains unchanged. In Case II, the background magnetic field is time-dependent, whereas the plasma density is held fixed.

### 3. Simulation Results

#### 3.1. Case I: Role of Plasma Density Variations

In Case I, the plasma density varies slowly over time by modulating the weight of cold electrons, as detailed in Supporting Information S1. The density profile is given by:

$$n_0(t) = [0.62 - 0.38 \cos(\omega_0 t)] n_{e0}, \quad (2)$$

where  $\omega_0 = 2.75$  rad/s ( $\sim 438$  mHz) represents the modulation frequency, which is significantly lower than the typical frequency of chorus waves ( $\sim 10^4$  rad/s). Figure 1a presents the temporal variation of  $n_0$ , exhibiting a sinusoidal modulation with a period of  $\sim 2.3$  s. The plasma density decreases to as low as 25% of the nominal value of  $5 \text{ cm}^{-3}$ , comparable to satellite observations that report reductions down to  $\sim 20\%$  (Haque et al., 2011; W. Li, Bortnik, et al., 2011).

Throughout the simulation, the background magnetic field remains unchanged over time, with an equatorial magnitude of  $B_{e0} = 144$  nT. The ratio of the electron plasma frequency  $\omega_{pe} = \sqrt{n_0 e^2 / m_e \epsilon_0}$  (where  $\epsilon_0$  is the vacuum permittivity) to the equatorial electron gyrofrequency  $\Omega_{e0}$  varies between  $\omega_{pe}/\Omega_{e0} = 2.49$  and  $4.98$ . This range is consistent with the typical values observed in Earth's magnetosphere (R. Chen et al., 2021; Fu et al., 2014; Yue et al., 2016).

Figures 1b and 1c show the temporal evolution of the perpendicular wave magnetic field component  $\delta B_{\perp 1}$  and the wave spectrum defined as  $\delta B = \sqrt{\delta B_{\perp 1}^2 + \delta B_{\perp 2}^2}$  at  $\lambda = 4^\circ$ , where “ $\perp 1$ ” and “ $\perp 2$ ” correspond to the radial and azimuthal directions, respectively. Chorus bursts, indicated by the white solid arrow in Figure 1c, are self-consistently excited by energetic electrons and exhibit alternating “on-off” modulation synchronized with plasma density variations at a period of  $\sim 2.3$  s. During the “on” stage near  $n_0$  peaks, the bursts consist of discrete rising-tone elements, with peak amplitudes reaching  $\delta B/B_{e0} \sim 0.015$  and average frequency chirping rates of  $\partial \omega / \partial t \sim 3.1 \times 10^{-4} \Omega_{e0}^2$  (equivalent to  $\sim 31.9$  kHz/s). These quasi-periodic elements are characterized by a period of  $\sim 0.31$  s and result from continuous injections of energetic electrons (R. Chen et al., 2025; Gao et al., 2022; Lu et al., 2021).

Each chorus element is initiated at a low frequency near  $\sim 0.2$ – $0.25 \Omega_{e0}$ , where its spectrum connects to whistler waves with weak amplitudes of  $\delta B/B_{e0} \sim 0.002$ , as indicated by the white hollow arrow in Figure 1c. Unlike rapidly chirping chorus elements, whistler waves exhibit slow frequency variations as plasma density changes, increasing from  $\sim 0.2 \Omega_{e0}$  at  $n_0 = 5 \text{ cm}^{-3}$  to  $\sim 0.3 \Omega_{e0}$  at  $n_0 = 1.25 \text{ cm}^{-3}$ . Similar wave behavior is also seen at other latitudes (not shown).

Chorus waves are triggered through nonlinear interactions with energetic electrons, while whistler waves arise from the linear instability. To demonstrate this distinction, we calculate frequency  $\omega_L$  corresponding to the maximum linear growth rate using the BO dispersion relation solver (Xie, 2019), with details in Figure 2b. As shown by the white curve in Figure 1c,  $\omega_L$  varies with time. The simulated whistler wave frequencies closely

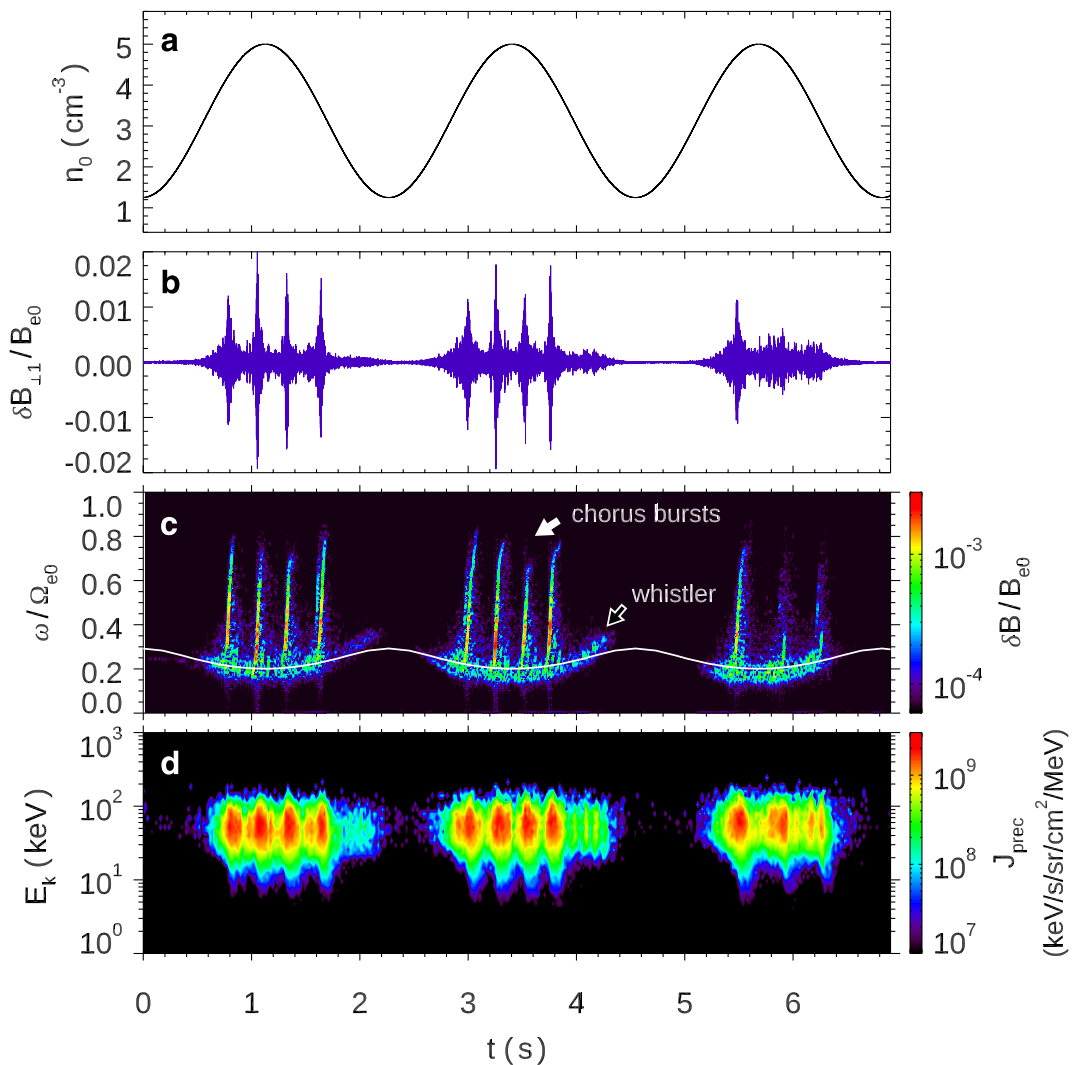


**Figure 1.** Case I: modulation of chorus waves and electron precipitation due to plasma density variations. (a) Temporal variation of  $n_0$ . (b)  $\delta B_{\perp\perp} / B_{e0}$  waveform and (c)  $\delta B$  spectrum at  $\lambda = 4^\circ$ . The white curve represents the frequency  $\omega_L$  corresponding to the maximum linear growth rate. The white hollow arrow marks chorus bursts, and the white solid arrow denotes whistler waves. (d) Differential energy flux of precipitating electrons  $J_{\text{prec}}$  at  $\lambda_{FT}^S$ .

follow  $\omega_L$ , with minor discrepancies attributed to the assumption of a fixed velocity distribution for energy electrons. In contrast, chorus waves span a broader and higher frequency range than  $\omega_L$ , indicating a nonlinear growth mechanism, as further supported by the theoretical analysis in Figure 2.

Electron holes in velocity phase space, which are characteristic signatures of nonlinear wave-particle interactions (Omura, 2021; Wang et al., 2024), are observed along with chorus elements (Figure S2 in Supporting Information S1), but are absent for whistler waves, reinforcing different generation mechanisms. The amplitude variations further reveal two distinct growth stages for whistler and chorus waves, namely a linear stage and a nonlinear stage. Quantification of the growth rates shows that the nonlinear stage has a much higher rate than the linear stage, consistent with the theoretical analysis presented later in Figure 2b. Additional details are provided in Figure S3 of Supporting Information S1.

Through cyclotron resonance, electrons that counter-propagate with waves are scattered into the loss cone, resulting in precipitation (Kasahara et al., 2018; Miyoshi, Oyama, et al., 2015; Miyoshi, Saito, et al., 2015; Miyoshi et al., 2020; Nishimura et al., 2010). Figure 1d illustrates the differential energy flux of precipitating electrons  $J_{\text{prec}}$  at the southern magnetic footprint  $\lambda_{FT}^S$ . Electrons with kinetic energies in the range of

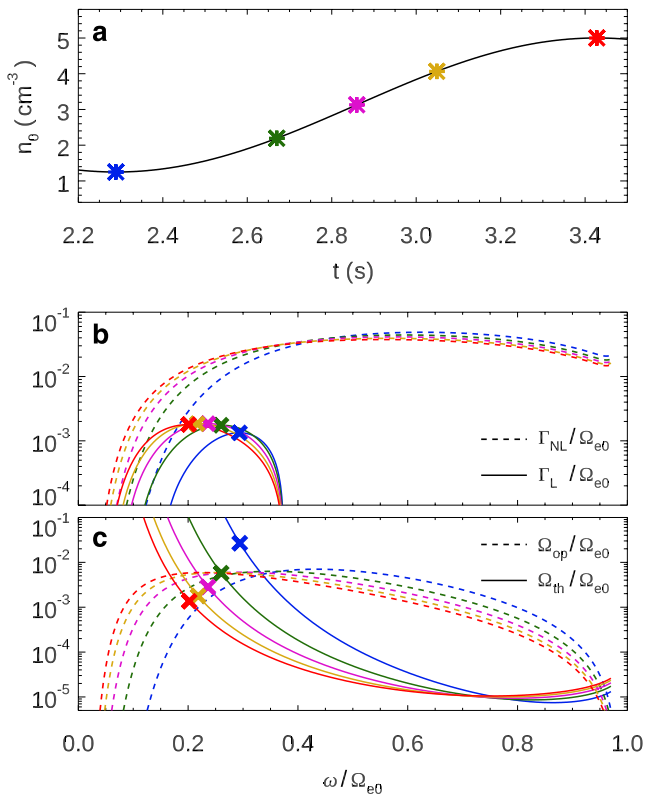


**Figure 2.** Theoretical analysis of wave growth dependence on plasma density variations. (a) Zoomed-in plot of  $n_0(t)$ . Five selected  $n_0$  values are marked by colored asterisks:  $1.25 \text{ cm}^{-3}$  (minimum, blue),  $2.19 \text{ cm}^{-3}$  (first quartile, green),  $3.13 \text{ cm}^{-3}$  (median, magenta),  $4.06 \text{ cm}^{-3}$  (third quartile, orange), and  $5.0 \text{ cm}^{-3}$  (maximum, red). (b) Linear growth rate  $\Gamma_L$  (solid curves) and nonlinear growth rate  $\Gamma_{NL}$  for the optimum amplitudes (dotted curves) as a function of  $\omega$ . Colors represent different  $n_0$  values and crosses mark the frequencies  $\omega_L$ . (c) Threshold amplitude  $\Omega_{th}$  (solid curves) and optimum amplitude  $\Omega_{op}$  (dotted curves) as a function of  $\omega$  for the same set of  $n_0$  values. Crosses mark  $\Omega_{th}$  at  $\omega_L$ .

$E_k \sim 10\text{--}200 \text{ keV}$  are precipitated, with the peak intensity of  $J_{prec} \sim 3 \times 10^9 \text{ keV/s/sr/cm}^2/\text{MeV}$ , comparable to observations from the Electron Losses and Fields Investigation (ELFIN) CubeSats at  $\sim 450 \text{ km}$  altitude, which reported  $J_{prec} \sim 6 \times 10^9 \text{ keV/s/sr/cm}^2/\text{MeV}$  at  $63 \text{ keV}$  (Shen et al., 2023; Zhang et al., 2022, 2023). The precipitation flux shows a one-to-one correspondence with individual chorus elements, and its intensity is positively correlated with wave amplitude. Therefore, electron precipitation also exhibits “on-off” modulation with periods of  $\sim 2.3 \text{ s}$ , consistent with that observed in pulsating aurora. Energy dispersion is also present, in agreement with the observations from the LEO satellite Reimei (Miyoshi, Saito, et al., 2015).

A theoretical analysis is conducted to investigate how plasma density variations influence both linear and nonlinear wave growth. Figure 2a shows a zoomed-in plot of the temporal evolution of  $n_0$ , with five representative values marked by colored asterisks:  $1.25 \text{ cm}^{-3}$  (minimum, blue),  $2.19 \text{ cm}^{-3}$  (first quartile, green),  $3.13 \text{ cm}^{-3}$  (median, magenta),  $4.06 \text{ cm}^{-3}$  (third quartile, orange), and  $5.0 \text{ cm}^{-3}$  (maximum, red). Figure 2b presents the linear growth rate  $\Gamma_L$  (solid curves) as a function of wave frequency  $\omega$ , calculated from the initial energetic electron velocity distribution to characterize whistler-wave excitation. The variation in energetic electron number density is negligible, as precipitating electrons constitute only  $\sim 0.5\%$  of the population. The curves are color-coded by the corresponding  $n_0$  values, and the crosses mark the frequencies  $\omega_L$  where  $\Gamma_L$  peaks. As  $n_0$  increases,  $\omega_L$  decreases from  $\sim 0.3 \Omega_{e0}$  to  $\sim 0.2 \Omega_{e0}$ . The peak  $\Gamma_L$  reaches  $\sim 2 \times 10^{-3} \Omega_{e0}$  at higher  $n_0$  but drops to  $\sim 1 \times 10^{-3} \Omega_{e0}$  when  $n_0 = 1.25 \text{ cm}^{-3}$ , explaining the weak whistler wave amplitudes near density troughs (Figure 1c).

Nonlinear theory indicates that chorus wave excitation requires seed waves generated from linear instability at the frequency  $\omega_L$ , typically in the form of whistler waves (Nogi & Omura, 2023; Omura, 2021). Nonlinear growth is initiated once the seed wave amplitude exceeds a threshold and continues until the amplitude reaches an optimum

value, at which point the triggering process terminates (Omura, 2021). The threshold and optimum amplitudes thus define the lower and upper bounds of wave amplitude during nonlinear growth, respectively (Katoh et al., 2018). Figure 2b presents the nonlinear growth rate  $\Gamma_{NL}$  (dotted curves), calculated using Equation (92) in Omura (2021) based on the optimum amplitude. By definition,  $\Gamma_{NL}$  is inversely proportional to  $\sqrt{\delta B}$ . It is found that even at the upper amplitude bound, which yields the minimum  $\Gamma_{NL}$ , the nonlinear growth rate ( $\sim 10^{-2}\Omega_{e0}$ ) remains an order of magnitude higher than the linear growth rate, supporting the larger amplitude of chorus waves compared to whistler waves in the simulation.

Figure 2c presents the threshold amplitude  $\Omega_{th}$  (solid curves) and optimum amplitude  $\Omega_{op}$  (dotted curves) for selected  $n_0$  values, calculated using Equations (105) and (97) in Omura (2021), respectively. Crosses indicate the values of  $\Omega_{th}$  at  $\omega_L$ . At higher  $n_0$ ,  $\Omega_{th}$  at  $\omega_L$  decreases with increasing plasma density and is lower than the corresponding  $\Omega_{op}$ , indicating that nonlinear growth can be easily triggered, as a moderate increase in seed wave amplitude is sufficient to exceed the threshold. Meanwhile,  $\Omega_{th}/\Omega_{e0} < \delta B/B_{e0} < \Omega_{op}/\Omega_{e0}$  is satisfied, as shown in Figure S4 of Supporting Information S1. In contrast, at lower  $n_0$  (e.g.,  $n_0 = 1.25 \text{ cm}^{-3}$ ), the condition  $\Omega_{th} < \Omega_{op}$  is not satisfied at  $\omega_L$ , thereby preventing the nonlinear growth. This quantification demonstrates that the chorus modulation due to plasma density variations is determined by nonlinear wave-particle interactions.

### 3.2. Case II: Role of Compressional Magnetic Field Fluctuations

In Case II, a slowly varying compressional magnetic field is artificially superimposed on the dipole field (Coroniti & Kennel, 1970; W. Li, Thorne, et al., 2011; L. Li et al., 2023; Xia et al., 2020), with further description provided in Supporting Information S1. The total background magnetic field is defined as:

$$\mathbf{B}_0(t) = [1.1 + 0.1 \cos(\omega_0 t)] \mathbf{B}_{dip}, \quad (3)$$

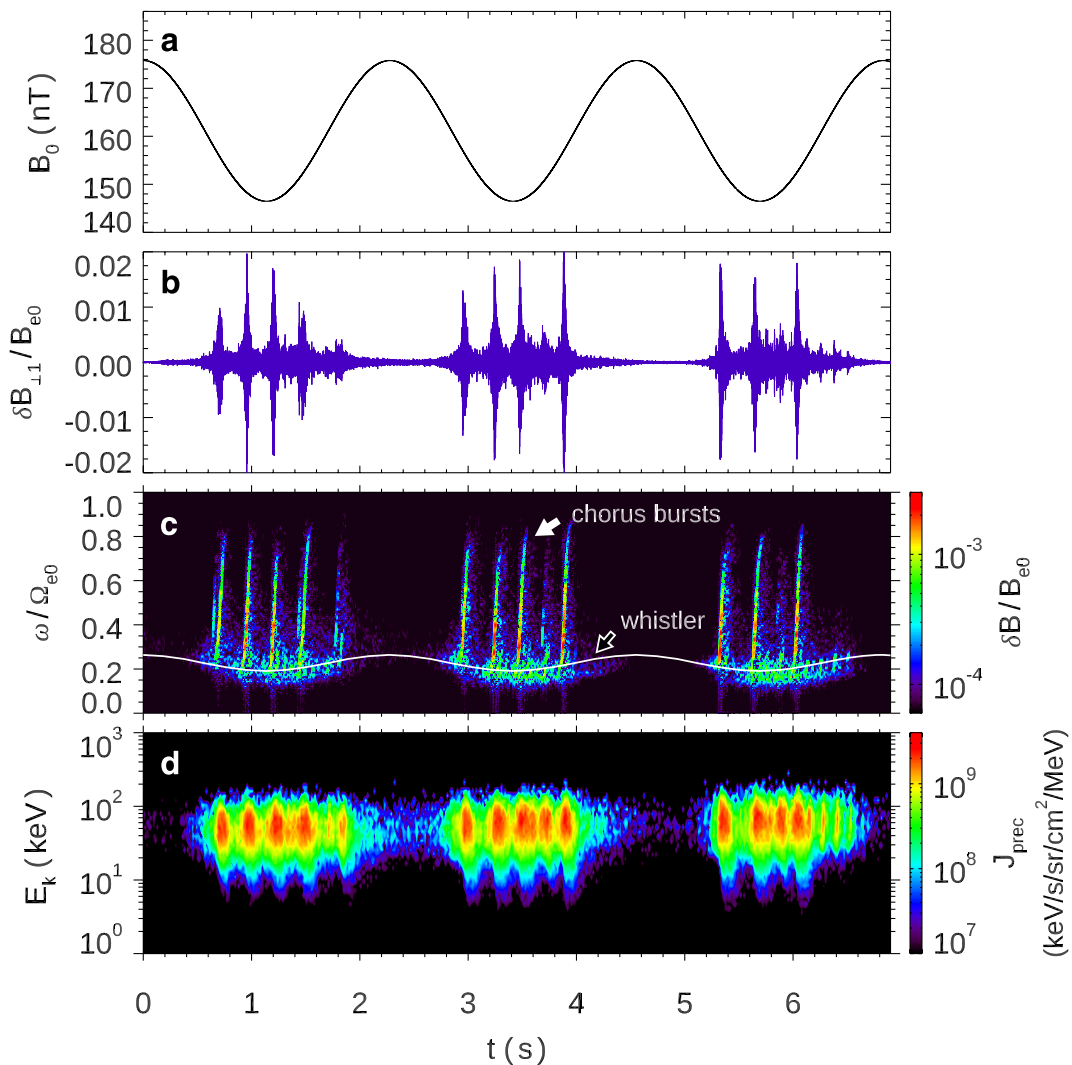
where  $\omega_0 = 2.75 \text{ rad/s}$  is the modulation frequency. The induced electric field resulting from the slow variation of  $\mathbf{B}_0$  is neglected, as  $\omega_0$  is much smaller than the chorus frequency.

Figure 3a shows the temporal variation of  $B_0$  at  $\lambda = 4^\circ$ , exhibiting sinusoidal modulation with a period of  $\sim 2.3 \text{ s}$ . The  $B_0$  value increases by 20% relative to its nominal value at this latitude (from 146.5 to 175.8 nT), consistent with the observed enhancement in the magnetosphere (L. Li et al., 2023). The plasma density  $n_0 = 5 \text{ cm}^{-3}$  is unchanged throughout the simulation. Under this configuration,  $\omega_{pe}/\Omega_{e0}$  changes from 4.16 to 4.98.

Figures 3b and 3c show the  $\delta B_{\perp 1}$  waveform and the  $\delta B$  spectrum at  $\lambda = 4^\circ$ . Chorus bursts (indicated by the white solid arrow) are modulated by compressional magnetic field fluctuations, with bursts concentrated near magnetic field troughs. The rising-tone elements within the bursts are characterized by average chirping rates of  $\partial\omega/\partial t \sim 3.0 \times 10^{-4}\Omega_{e0}^2$  (equivalent to  $\sim 31.1 \text{ kHz/s}$ ) and average periods of  $\sim 0.29 \text{ s}$ . Each chorus element connects spectrally to low-frequency, weak-amplitude whistler waves (indicated by the white hollow arrow). The frequency of these whistler waves matches  $\omega_L$ , which varies with the background magnetic field, being  $\sim 0.2 \Omega_{e0}$  at  $B_0$  troughs and increasing to  $\sim 0.3 \Omega_{e0}$  at  $B_0$  peaks.

Figure 3d presents the differential energy flux of electron precipitation  $J_{prec}$  at  $\lambda_{FT}^S$ . The precipitation intensity also exhibits modulation synchronized with  $B_0$  fluctuations. Electrons within  $E_k = \sim 10\text{--}200 \text{ keV}$  are precipitated, and the peak intensity reaches  $J_{prec} \sim 4 \times 10^9 \text{ keV/s/sr/cm}^2/\text{MeV}$ , also consistent with ELFIN observations (Shen et al., 2023; Zhang et al., 2023).

The effects of compressional magnetic field fluctuations are examined through theoretical analysis. Figure 4a presents a zoomed-in plot of  $B_0(t)$  at  $\lambda = 4^\circ$ , with five representative  $B_0$  values marked by asterisks: 175.8 nT (maximum, blue), 168.4 nT (third quartile, green), 161.1 nT (median, magenta), 153.7 nT (first quartile, orange), and 146.5 nT (minimum, red). Figure 4b shows the corresponding linear growth rates  $\Gamma_L$  (solid curves) for waves under these magnetic field conditions. The crosses denote the peak  $\Gamma_L$  at frequency  $\omega_L$ . The peak  $\Gamma_L$ , on the order of  $\sim 10^{-3}\Omega_{e0}$ , exhibits a weak negative correlation with  $B_0$ , consistent with weaker whistler amplitude near magnetic field peaks. While the nonlinear growth rates  $\Gamma_{NL}$  (dotted curves in Figure 4b), with peak values of  $\sim 10^{-2}\Omega_{e0}$ , are typically one order of magnitude higher and are considered responsible for chorus excitation. For simplicity,  $\Gamma_L$  and  $\Gamma_{NL}$  are calculated using the initial velocity distribution of energetic electrons, despite a slight increase in their temperature anisotropy with increasing  $B_0$ . To confirm robustness, we repeated the calculation



**Figure 3.** Case II: modulation of chorus waves and electron precipitation due to compressional magnetic field fluctuations. (a) Temporal variation of  $B_0$  at  $\lambda = 4^\circ$ . (b–d) Same format as Figures 1b–1d.

with the time-dependent temperature anisotropy (Figure S5 in Supporting Information S1), and the main conclusions remain unchanged.

Figure 4c further presents the threshold amplitude  $\Omega_{\text{th}}$  and optimum amplitude  $\Omega_{\text{op}}$ , with crosses marking  $\Omega_{\text{th}}$  at  $\omega_L$ . The condition for nonlinear wave growth is sensitive to magnetic field fluctuations. At lower  $B_0$ , the condition  $\Omega_{\text{th}} < \Omega_{\text{op}}$  is satisfied at  $\omega_L$ , allowing chorus waves to be triggered via nonlinear wave-particle interactions, with  $\delta B / B_{e0}$  estimated to lie between  $\Omega_{\text{th}} / \Omega_{e0}$  and  $\Omega_{\text{op}} / \Omega_{e0}$  (not shown). While at higher  $B_0$ ,  $\Omega_{\text{th}} > \Omega_{\text{op}}$ , consistent with the absence of chorus waves near magnetic field peaks. Therefore, chorus modulation due to compressional magnetic field fluctuations is also determined by nonlinear effects.

#### 4. Discussions

In this study, the simulated chorus bursts are found near plasma density peaks (Figure 1c) or magnetic field troughs (Figure 3c), consistent with modulation patterns reported in observations (Moullard et al., 2002; Figures 4–5 in W. Li, Bortnik, et al., 2011; Figures 2 and 6 in W. Li, Thorne, et al., 2011; Figure 2 in L. Li et al., 2023). These patterns are also supported by nonlinear theory, which demonstrates that the condition for nonlinear wave growth depends sensitively on background plasma parameters. However, other observational events indicated chorus bursts near plasma density troughs (Figures 2–3 in W. Li, Bortnik, et al., 2011) or magnetic field peaks

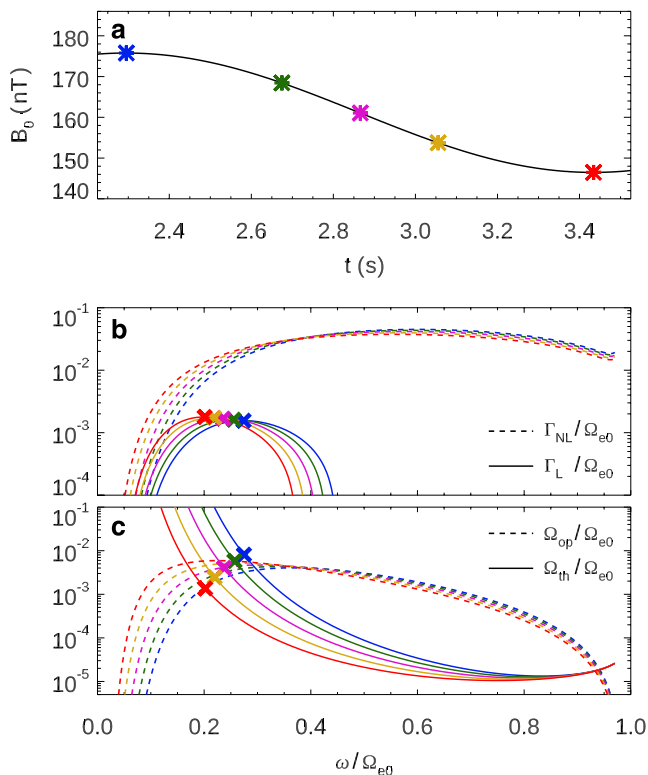


**Figure 4.** Theoretical analysis of wave growth dependence on compressional magnetic field fluctuations. (a) Zoomed-in plot of  $B_0(t)$  at  $\lambda = 4^\circ$ . Five selected  $B_0$  values are marked by colored asterisks: 175.8 nT (maximum, blue), 168.4 nT (third quantile, green), 161.1 nT (median, magenta), 153.7 nT (first quantile, orange), and 146.5 nT (minimum, red). (b–c) Same format as Figures 2b and 2c.

(Figure 3 in L. Li et al., 2023). To address these discrepancies, specific information on the plasma parameters for these events is required. As the next step, we will carry out a systematic parametric simulation study, which is valuable for investigating the effects of  $\omega_{pe}/\Omega_{e0}$  on both linear and nonlinear growth. In the linear stage, the growth rate depends on  $\omega_{pe}/\Omega_{e0}$ , and the relationship between the linear-stage saturation amplitude and the nonlinear threshold amplitude also varies with it. In the nonlinear growth stage, the wave amplitude lies between the threshold and optimum amplitudes, both of which are associated with  $\omega_{pe}/\Omega_{e0}$ .

Coroniti and Kennel (1970) introduced the concept of diffusive equilibrium to describe electron precipitation driven by weak whistler-mode waves through diffusion. In their framework, the wave-particle system reaches a steady state characterized by a balance between the wave growth rate induced by resonant electrons and the convective loss rate of waves (see their Equation (6)). Under such conditions, the electron loss rate caused by wave scattering is identical to the electron injection rate. In this study, the convective loss rate of whistler-mode waves is estimated as  $v_g/\ell = 4.3 \times 10^{-3}\Omega_{e0}$ , where  $v_g$  is the wave group velocity, with an average value of  $\sim 0.5 V_{Ae0}$  over 0.2–0.8  $\Omega_{e0}$ , and  $\ell$  is the source region length, approximated as  $\sim 5^\circ$  near the magnetic equator (Taubenschuss et al., 2016), corresponding to  $\sim 450 V_{Ae0}/\Omega_{e0}$ . For weak whistler-mode waves near plasma density troughs and magnetic field peaks, the linear growth rate ( $\sim 2 \times 10^{-3}\Omega_{e0}$ ) is comparable with the convective loss rate. Consequently, the associated electron scattering can be interpreted as a diffusive equilibrium process. In contrast, near plasma density peaks and magnetic field troughs, the nonlinear growth rate of chorus waves ( $\sim 10^{-2}\Omega_{e0}$ ) is much larger. Here, wave amplification and the resulting electron scattering are dominated by nonlinear wave-particle interactions.

Pulsating aurora typically exhibits three types of modulation: a main modulation on timescales of several seconds (Anderson & Milton, 1964; Nishimura et al., 2010), an internal modulation around  $\sim 0.3$  s (Hosokawa et al., 2020; Miyoshi, Saito, et al., 2015), and a fast modulation below 0.1 s (R. Chen et al., 2024). In addition to reproducing the main modulation in electron precipitation, our simulations also capture the internal modulation ( $\sim 0.29$  s;

Figures 1d and 3d) caused by each chorus element, which is attributed to energetic particle injections. The fast modulation has also been reproduced in a separate simulation study (H. Chen et al., 2025), and its mechanism remains to be investigated.

While both simulation cases reproduce the modulation of electron precipitation with similar periods (~2.3 s), there are subtle differences in the precipitation intensity. Case II, driven by compressional magnetic field fluctuations, yields a slightly higher peak flux ( $\sim 4 \times 10^9$  keV/s/sr/cm $^2$ /MeV) compared to Case I ( $\sim 3 \times 10^9$  keV/s/sr/cm $^2$ /MeV). This difference may be attributed to stronger wave amplitudes achieved near magnetic field troughs in Case II, which enhance wave-particle interactions. A comparison of electron precipitation characteristics across different background parameters would be valuable for future studies.

In this study, electron precipitation is driven by cyclotron resonance with parallel chorus waves. While Landau resonance with oblique waves can also contribute to pitch-angle scattering (H. Chen et al., 2024; da Silva et al., 2018; Hsieh & Omura, 2023; Wang et al., 2024), investigating this effect requires two-dimensional simulations, which is beyond the scope of the present work and will be addressed in future studies. To further clarify the nonlinear physics involved in precipitation, the dynamics of precipitating electrons need to be examined, which can be achieved using the particle tracking method described by H. Chen et al. (2024). Although the present modulation is demonstrated in a reduced system, similar modulation can also be reproduced in real-size magnetospheric simulations under appropriate plasma parameters. H. Chen (2025) demonstrated that the precipitation energy range in real-size simulations is consistent with that in reduced systems and also exhibits energy-dispersive signatures.

## 5. Summary

By performing self-consistent PIC simulations with typical magnetospheric plasma parameters, we reproduce the modulation of chorus waves on timescales of several seconds, driven by plasma density variations and compressional magnetic field fluctuations. We demonstrate that chorus modulation is determined by nonlinear wave-particle interactions, where the condition for nonlinear wave growth is highly sensitive to background plasma parameters. Nonlinear growth occurs only within a specific range where the threshold amplitude is lower than the optimum amplitude.

Electron precipitation in the ~10–200 keV range, driven by modulated chorus waves, also exhibits several-second periods, consistent with the main modulation observed in pulsating aurora. The precipitation flux shows a one-to-one correspondence with individual chorus elements, with peak intensities reaching  $\sim 10^9$  keV/s/sr/cm $^2$ /MeV, in agreement with typical observational measurements.

## Data Availability Statement

The data used to reproduce the figures in this manuscript are publicly available at H. Chen (2025).

## Acknowledgments

This work was supported by the NASA Grant 80NSSC21K1688 and the NSF Grant AGS-2453814. LC was supported by the NSF Grant AGS-2225121. YO and YH were supported by JSPS KAKENHI Grant JP20H01960 and JP23H05429.

## References

- Agapitov, O., Mourenas, D., Artemyev, A., Mozer, F. S., Bonnell, J. W., Angelopoulos, V., et al. (2018). Spatial extent and temporal correlation of chorus and hiss: Statistical results from multipoint THEMIS observations. *Journal of Geophysical Research: Space Physics*, 123(10), 8317–8330. <https://doi.org/10.1029/2018JA025725>
- Albertson, V. D., & Thorson, J. M. (1974). Power system disturbances during A-K-8 geomagnetic storm: August 4, 1972. *IEEE Transactions on Power Apparatus and Systems*, PAS-93(4), 1025–1030. <https://doi.org/10.1109/TPAS.1974.294046>
- Anderson, K. A., & Milton, D. W. (1964). Balloon observations of X rays in the auroral zone: 3. In *High time resolution studies*. <https://doi.org/10.1029/JZ069i021p04457>
- Benson, R. F. (1960). Effect of line-of-sight aurora on radio star scintillations. *Journal of Geophysical Research*, 65(7), 1981–1985. <https://doi.org/10.1029/JZ065i007p01981>
- Boteler, D. H. (2019). A 21st century view of the March 1989 magnetic storm. *Space Weather*, 17(10), 1427–1441. <https://doi.org/10.1029/2019SW002278>
- Burtis, W. J., & Helliwell, R. A. (1969). Banded chorus a new type of VLF radiation observed in the magnetosphere by OGO 1 and OGO 3. *Journal of Geophysical Research*, 74(11), 3002–3010. <https://doi.org/10.1029/JA074i011p03002>
- Chen, H. (2025). Database of “Modulation of chorus waves and associated electron precipitation: A simulation study” [Dataset]. Zenodo. <https://doi.org/10.5281/zenodo.15815496>
- Chen, H., Wang, X., Chen, L., Omura, Y., Tsurutani, B. T., Lin, Y., & Xia, Z. (2023). Evolution of chorus subpackets in the Earth's magnetosphere. *Geophysical Research Letters*, 50(21), e2023GL105938. <https://doi.org/10.1029/2023GL105938>
- Chen, H., Wang, X., Li, X., Chen, R., Chen, L., Omura, Y., et al. (2025). Quantifying electron precipitation driven by chorus waves using self-consistent particle-in-cell simulations. *Geophysical Research Letters*, e2025GL116478. <https://doi.org/10.1029/2025GL116478>

- Chen, H., Wang, X., Zhao, H., Lin, Y., Chen, L., Omura, Y., et al. (2024). Electron dynamics associated with advection and diffusion in self-consistent wave-particle interactions with oblique chorus waves. *Geophysical Research Letters*, 51(14), e2024GL110362. <https://doi.org/10.1029/2024GL110362>
- Chen, L., Breneman, A. W., Xia, Z., & Zhang, X.-J. (2020). Modeling of bouncing electron microbursts induced by ducted chorus waves. *Geophysical Research Letters*, 47(17), e2020GL089400. <https://doi.org/10.1029/2020GL089400>
- Chen, R., Gao, X., Lu, Q., Chen, L., Tsurutani, B. T., Li, W., et al. (2021). In situ observations of whistler-mode chorus waves guided by density ducts. *Journal of Geophysical Research: Space Physics*, 126(4), e2020JA028814. <https://doi.org/10.1029/2020JA028814>
- Chen, R., Miyoshi, Y., Gao, X., Lu, Q., Tsurutani, B. T., Hosokawa, K., et al. (2024). Observational evidence for three time-scale modulations in the pulsating aurora. *Geophysical Research Letters*, 51(16), e2024GL108253. <https://doi.org/10.1029/2024GL108253>
- Chen, R., Miyoshi, Y., Zhao, H., Chen, H., Wang, X., Kasahara, Y., et al. (2025). Observational evidence for the nonlinear growth of chorus waves caused by substorm injected energetic electrons. *Journal of Geophysical Research: Space Physics*, 130(7), e2025JA033931. <https://doi.org/10.1029/2025JA033931>
- Chernous, S. A., Shagimuratov, I. I., Ievenko, I. B., Filatov, M. V., Efishev, I. I., Shvets, M. V., & Kalitenkov, N. V. (2018). Auroral perturbations as an indicator of ionosphere impact on navigation signals. *Russian Journal of Physical Chemistry B*, 12(3), 562–567. <https://doi.org/10.1134/S1990793118030065>
- Coroniti, F. V., & Kennel, C. F. (1970). Electron precipitation pulsations. *Journal of Geophysical Research*, 75(7), 1279–1289. <https://doi.org/10.1029/JA075i007p01279>
- da Silva, C. L., Denton, R. E., Hudson, M. K., Millan, R. M., Liu, K., & Bortnik, J. (2018). Test-particle simulations of linear and nonlinear interactions between a 2-D whistler-mode wave packet and radiation belt electrons. *Geophysical Research Letters*, 45(11), 5234–5245. <https://doi.org/10.1029/2018GL077877>
- Demekhov, A. G., Taubenschuss, U., Hanzelka, M., & Santolík, O. (2020). Frequency dependence of very low frequency chorus Poynting flux in the source region: THEMIS observations and a model. *Geophysical Research Letters*, 47(6), e2020GL086958. <https://doi.org/10.1029/2020GL086958>
- Denton, R. E., Menietti, J. D., Goldstein, J., Young, S. L., & Anderson, R. R. (2004). Electron density in the magnetosphere. *Journal of Geophysical Research*, 109(A9), A09215. <https://doi.org/10.1029/2003JA010245>
- Escoubet, C. P., Pedersen, A., Schmidt, R., & Lindqvist, P. A. (1997). Density in the magnetosphere inferred from ISEE 1 spacecraft potential. *Journal of Geophysical Research*, 102(A8), 17595–17609. <https://doi.org/10.1029/97JA00290>
- Fu, X., Cowee, M. M., Friedel, R. H., Funsten, H. O., Gary, S. P., Hospodarsky, G. B., et al. (2014). Whistler anisotropy instabilities as the source of banded chorus: Van Allen Probes observations and particle-in-cell simulations. *Journal of Geophysical Research: Space Physics*, 119(10), 8288–8298. <https://doi.org/10.1002/2014JA020364>
- Gan, L., Li, W., Ma, Q., Albert, J. M., Artemyev, A. V., & Bortnik, J. (2020). Nonlinear interactions between radiation belt electrons and chorus waves: Dependence on wave amplitude modulation. *Geophysical Research Letters*, 47(4), e2019GL085987. <https://doi.org/10.1029/2019GL085987>
- Gao, X., Chen, R., Lu, Q., Chen, L., Chen, H., & Wang, X. (2022). Observational evidence for the origin of repetitive chorus emissions. *Geophysical Research Letters*, 49(12), e2022GL099000. <https://doi.org/10.1029/2022GL099000>
- Gao, X., Li, W., Thorne, R. M., Bortnik, J., Angelopoulos, V., Lu, Q., et al. (2014). New evidence for generation mechanisms of discrete and hiss-like whistler mode waves. *Geophysical Research Letters*, 41(14), 4805–4811. <https://doi.org/10.1002/2014GL060707>
- Gao, X., Ma, J., Shao, T., Chen, R., Ke, Y., & Lu, Q. (2023). Why chorus waves are the dominant driver for diffuse auroral precipitation. *Science Bulletin*, 69(5), 597–600. <https://doi.org/10.1016/j.scib.2023.12.009>
- Hanzelka, M., & Santolík, O. (2023). Theories of growth and propagation of parallel whistler-mode chorus emissions: A review. *Surveys in Geophysics*, 45(1), 1–54. <https://doi.org/10.1007/s10712-023-09792-x>
- Haque, N., Inan, U. S., Bell, T. F., Pickett, J. S., Trotignon, J. G., & Faszkó, G. (2011). Cluster observations of whistler mode ducts and banded chorus. *Geophysical Research Letters*, 38(18), L18107. <https://doi.org/10.1029/2011GL049112>
- Horne, R. B., & Thorne, R. M. (1998). Potential waves for relativistic electron scattering and stochastic acceleration during magnetic storms. *Geophysical Research Letters*, 25(15), 3011–3014. <https://doi.org/10.1029/98GL01002>
- Hosokawa, K., Miyoshi, Y., Ozaki, M., Oyama, S.-I., Ogawa, Y., Kurita, S., et al. (2020). Multiple time-scale beats in aurora: Precise orchestration via magnetospheric chorus waves. *Scientific Reports*, 10(1), 3380. <https://doi.org/10.1038/s41598-020-59642>
- Hsieh, Y.-K., & Omura, Y. (2023). Precipitation rates of electrons interacting with lower-band chorus emissions in the inner magnetosphere. *Journal of Geophysical Research: Space Physics*, 128(6), e2023JA031307. <https://doi.org/10.1029/2023JA031307>
- Hu, G., & Krommes, J. A. (1994). Generalized weighting scheme for 3D particle-simulation method. *Physics of Plasmas*, 1(4), 863–874. <https://doi.org/10.1063/1.870745>
- Jaynes, A. N., Lessard, M. R., Takahashi, K., Ali, A. F., Malaspina, D. M., Michell, R. G., et al. (2015). Correlated Pc4–5 ULF waves, whistler-mode chorus, and pulsating aurora observed by the Van Allen Probes and ground-based systems. *Journal of Geophysical Research: Space Physics*, 120(10), 8749–8761. <https://doi.org/10.1002/2015JA021380>
- Kang, N., Bortnik, J., Zhang, X., Claudepierre, S., & Shi, X. (2022). Relativistic microburst scale size induced by a single point-source chorus element. *Geophysical Research Letters*, 49(23), e2022GL100841. <https://doi.org/10.1029/2022GL100841>
- Kasahara, S., Miyoshi, Y., Yokota, S., Mitani, T., Kasahara, Y., Matsuda, S., et al. (2018). Pulsating aurora from electron scattering by chorus waves. *Nature*, 554(7692), 337–340. <https://doi.org/10.1038/nature25505>
- Katoh, Y., Omura, Y., Miyake, Y., Usui, H., & Nakashima, H. (2018). Dependence of generation of whistler mode chorus emissions on the temperature anisotropy and density of energetic electrons in the Earth's inner magnetosphere. *Journal of Geophysical Research: Space Physics*, 123(2), 1165–1177. <https://doi.org/10.1002/2017JA024801>
- Ke, Y., Lu, Q., Gao, X., Chen, H., & Chen, R. (2022). Ray-tracing simulations of whistler-mode wave propagation in different rescaled dipole magnetic fields. *Earth Planetary Physics*, 6(6), 555–562. <https://doi.org/10.26464/epp2022048>
- Kellogg, P. J., & Monson, S. J. (1979). Radio emissions from the aurora. *Geophysical Research Letters*, 6(4), 297–300. <https://doi.org/10.1029/GL006i004p00297>
- Kong, Z., Gao, X., Lu, Q., Lei, W., Wang, X., Ma, J., et al. (2025). Modulation of electron precipitation regulated by electron injection: PIC simulations. *Physics of Plasmas*, 32(2), 022108. <https://doi.org/10.1063/5.0241061>
- Li, L., Omura, Y., Zhou, X.-Z., Zong, Q.-G., Rankin, R., Yue, C., et al. (2023). Chorus wave generation modulated by field line resonance and mirror-mode ULF waves. *Journal of Geophysical Research: Space Physics*, 128(2), e2022JA031127. <https://doi.org/10.1029/2022JA031127>
- Li, W., Bortnik, J., Thorne, R. M., Nishimura, Y., Angelopoulos, V., & Chen, L. (2011). Modulation of whistler mode chorus waves: 2. Role of density variations. *Journal of Geophysical Research*, 116(A6), A06206. <https://doi.org/10.1029/2010JA016313>

- Li, W., Thorne, R. M., Bortnik, J., Nishimura, Y., & Angelopoulos, V. (2011). Modulation of whistler mode chorus waves: 1. Role of compressional Pc4–5 pulsations. *Journal of Geophysical Research*, 116(A6), A06205. <https://doi.org/10.1029/2010JA016312>
- Lu, Q., Chen, L., Wang, X., Gao, X., Lin, Y., & Wang, S. (2021). Repetitive emissions of rising-tone chorus waves in the inner magnetosphere. *Geophysical Research Letters*, 48(15), e2021GL094979. <https://doi.org/10.1029/2021GL094979>
- Lu, Q., Ke, Y., Wang, X., Liu, K., Gao, X., Chen, L., & Wang, S. (2019). Two-dimensional general curvilinear particle-in-cell (gcPIC) simulation of rising-tone chorus waves in a dipole magnetic field. *Journal of Geophysical Research: Space Physics*, 124(6), 4157–4167. <https://doi.org/10.1029/2019ja026586>
- Miyoshi, Y., Hosokawa, K., Kurita, S., Oyama, S.-I., Ogawa, Y., Saito, S., et al. (2021). Penetration of MeV electrons into the mesosphere accompanying pulsating aurorae. *Scientific Reports*, 11(1), 13724. <https://doi.org/10.1038/s41598-021-92611-3>
- Miyoshi, Y., Oyama, S., Saito, S., Kurita, S., Fujiwara, H., Kataoka, R., et al. (2015). Energetic electron precipitation associated with pulsating aurora: EISCAT and Van Allen Probes observations. *Journal of Geophysical Research: Space Physics*, 120(4), 2754–2766. <https://doi.org/10.1002/2014ja020690>
- Miyoshi, Y., Saito, S., Kurita, S., Asamura, K., Hosokawa, K., Sakanoi, T., et al. (2020). Relativistic electron microbursts as high-energy tail of pulsating aurora electrons. *Geophysical Research Letters*, 47(21), e2020GL090360. <https://doi.org/10.1029/2020GL090360>
- Miyoshi, Y., Saito, S., Seki, K., Nishiyama, T., Kataoka, R., Asamura, K., et al. (2015). Relation between energy spectra of pulsating aurora electrons and frequency spectra of whistler-mode chorus waves. *Journal of Geophysical Research: Space Physics*, 120(9), 7728–7736. <https://doi.org/10.1002/2015JA021562>
- Moullard, O., Masson, A., Laakso, H., Parrot, M., Décréau, P., Santolik, O., et al. (2002). Density modulated whistler mode emissions observed near the plasmapause. *Geophysical Research Letters*, 29(20), 1975. <https://doi.org/10.1029/2002GL015101>
- Nishimura, Y., Bortnik, J., Li, W., Liang, J., Thorne, R. M., Angelopoulos, V., et al. (2015). Chorus intensity modulation driven by time-varying field-aligned low-energy plasma. *Journal of Geophysical Research: Space Physics*, 120(9), 7433–7446. <https://doi.org/10.1002/2015JA021330>
- Nishimura, Y., Bortnik, J., Li, W., Thorne, R. M., Lyons, L. R., Angelopoulos, V., et al. (2010). Identifying the driver of pulsating aurora. *Science*, 330(6000), 81–84. <https://doi.org/10.1126/science.1193186>
- Nishiyama, T., Miyoshi, Y., Katoh, Y., Sakanoi, T., Kataoka, R., & Okano, S. (2016). Substructures with luminosity modulation and horizontal oscillation in pulsating patch: Principal component analysis application to pulsating aurora. *Journal of Geophysical Research: Space Physics*, 121(3), 2360–2373. <https://doi.org/10.1002/2015JA022288>
- Nogi, T., & Omura, Y. (2023). Upstream shift of generation region of whistler-mode rising-tone emissions in the magnetosphere. *Journal of Geophysical Research: Space Physics*, 128(3), e2022JA031024. <https://doi.org/10.1029/2022JA031024>
- O'Brien, T. P., Lemon, C. L., & Blake, J. B. (2022). Electron precipitation curtains—Simulating the microburst origin hypothesis. *Journal of Geophysical Research: Space Physics*, 127(8), e2022JA030370. <https://doi.org/10.1029/2022JA030370>
- Omura, Y. (2021). Nonlinear wave growth theory of whistler-mode chorus and hiss emissions in the magnetosphere. *Earth Planets and Space*, 73(1), 1–28. <https://doi.org/10.1186/s40623-021-01380-w>
- Ozaki, M., Shiokawa, K., Miyoshi, Y., Hosokawa, K., Oyama, S., Yagitani, S., et al. (2018). Microscopic observations of pulsating aurora associated with chorus element structures: Coordinated Arase satellite-PWING observations. *Geophysical Research Letters*, 45(22), 12125–12134. <https://doi.org/10.1029/2018GL079812>
- Parker, S. E., & Lee, W. W. (1993). A fully nonlinear characteristic method for gyrokinetic simulation. *Physics of Fluids B*, 5(1), 77–86. <https://doi.org/10.1063/1.860870>
- Rasinskaite, D., Watt, C. E. J., Forsyth, C., Smith, A. W., Lao, C. J., Chakraborty, S., et al. (2025). Estimating electron temperature and density using Van Allen probe data: Typical behavior of energetic electrons in the inner magnetosphere. *Journal of Geophysical Research: Space Physics*, 130(4), e2024JA03443. <https://doi.org/10.1029/2024JA03443>
- Santolík, O., Kletzing, C. A., Kurth, W. S., Hopardasky, G. B., & Bounds, S. R. (2014). Fine structure of large-amplitude chorus wave packets. *Geophysical Research Letters*, 41(2), 293–299. <https://doi.org/10.1002/2013GL058889>
- Semeter, J., Mrak, S., Hirsch, M., Swoboda, J., Akbari, H., Starr, G., et al. (2017). GPS signal corruption by the discrete Aurora: Precise measurements from the Mahali experiment. *Geophysical Research Letters*, 44(19), 9539–9546. <https://doi.org/10.1002/2017GL073570>
- Shen, X.-C., Li, W., Capannolo, L., Ma, Q., Qin, M., Artemyev, A. V., et al. (2023). Modulation of energetic electron precipitation driven by three types of whistler mode waves. *Geophysical Research Letters*, 50(8), e2022GL101682. <https://doi.org/10.1029/2022GL101682>
- Taubenschuss, U., Santolík, O., Breuillard, H., Li, W., & Le Contel, O. (2016). Poynting vector and wave vector directions of equatorial chorus. *Journal of Geophysical Research: Space Physics*, 121(12), 11912–11928. <https://doi.org/10.1002/2016JA023389>
- Thorne, R. M., Ni, B., Tao, X., Horne, R. B., & Meredith, N. P. (2010). Scattering by chorus waves as the dominant cause of diffuse auroral precipitation. *Nature*, 467(7318), 943–946. <https://doi.org/10.1038/nature09467>
- Tsurutani, B. T., & Smith, E. J. (1974). Postmidnight chorus: A substorm phenomenon. *Journal of Geophysical Research*, 79(1), 118–127. <https://doi.org/10.1029/JA079i001p00118>
- Wang, X., Chen, H., Omura, Y., Hsieh, Y. K., Chen, L., Lin, Y., et al. (2024). Resonant electron signatures in the formation of chorus wave subpackets. *Geophysical Research Letters*, 51(8), e2023GL108000. <https://doi.org/10.1029/2023GL108000>
- Xia, Z., Chen, L., & Li, W. (2020). Statistical study of chorus modulations by background magnetic field and plasma density. *Geophysical Research Letters*, 47(22), e2020GL089344. <https://doi.org/10.1029/2020GL089344>
- Xie, H. S. (2019). BO: A unified tool for plasma waves and instabilities analysis. *Computer Physics Communications*, 244, 343–371. <https://doi.org/10.1016/j.cpc.2019.06.014>
- Yue, C., An, X., Bortnik, J., Ma, Q., Li, W., Thorne, R. M., et al. (2016). The relationship between the macroscopic state of electrons and the properties of chorus waves observed by the Van Allen Probes. *Geophysical Research Letters*, 43(15), 7804–7812. <https://doi.org/10.1002/2016GL070084>
- Zhang, X.-J., Angelopoulos, V., Artemyev, A., Mourenas, D., Agapitov, O., Tsai, E., & Wilkins, C. (2023). Temporal scales of electron precipitation driven by whistler-mode waves. *Journal of Geophysical Research: Space Physics*, 128(1), e2022JA031087. <https://doi.org/10.1029/2022JA031087>
- Zhang, X.-J., Angelopoulos, V., Mourenas, D., Artemyev, A., Tsai, E., & Wilkins, C. (2022). Characteristics of electron microburst precipitation based on high-resolution ELFIN measurements. *Journal of Geophysical Research: Space Physics*, 127(5), e2022JA030509. <https://doi.org/10.1029/2022JA030509>
- Zhang, X.-J., Chen, L., Artemyev, A. V., Angelopoulos, V., & Liu, X. (2019). Periodic excitation of chorus and ECH waves modulated by ultralow frequency compressions. *Journal of Geophysical Research: Space Physics*, 124(11), 8535–8550. <https://doi.org/10.1029/2019JA027201>